CHAPTER III

COMPUTATIONAL TECHNIQUES AND EXPERIMENTAL SETUP

3.1 Introduction

Details of the computational and experimental techniques used to calculate light scattering by dust particles is provided in this chapter. All important tools along with the steps involved in theoretical modeling approach has been discussed in the first section. In the second section details of the experimental setup is provided with specifications and function of each component. Alignment techniques of the optical components and validation procedure of the setup using spherical water droplets are also provided.

3.2 Computational techniques

A computational technique has been developed based on the software packages mentioned below, to compute and calculate light scattering properties of irregularly shaped aerosol and dust particles. The phase function $F_{11}(\theta)$ and degree of linear polarization $-F_{12}(\theta)/F_{11}(\theta)$ along with other scattering parameters were theoretically calculated using this technique.

The software packages are,

1. Blender 3D: Volumetric geometry design software for arbitrary shapes and materials used to model target geometries to replicate the particles employed in experimental characterization.
2. DDSCATCONVERT: Software package to convert the volumetric random shapes (in the form of a 3D triangular mesh) to dipole arrays by assigning dipoles to each point and vertices.
3. ParaView: Software available in the public domain to realize 3D targets generated in any technique as an array of constituting points. This is used to ensure proper target generation during the conversion of developed models to dipole arrays.
4. DDSCAT: The original FORTRAN DDA code to calculate scattering efficiencies and cross sections (scattering, absorption, polarization and extinction), asymmetry parameters, single scattering albedos and the sixteen elements of the Mueller matrix.
5. Post processing tool: An indigenously developed code in MATLAB© platform to facilitate the automatic averaging over a wide range of shape and size distributions using the DDSCAT generated computational calculations.

3.2.1 Blender 3D

The first step of the computational technique involves generation of targets for DDA simulations using different incident laser wavelengths. Blender is a software used to generate volumetric material targets for realistic investigation in modeling and simulation works (Figure 3.1 and 3.2). There are several advanced options provided in the software for target generation. In one procedure predefined algorithms can be used to develop random gaussian shapes. Another advantage is that targets can also be user defined or user modified in a manual mode. A primitive basis shape can be modified using shape and material modifiers. Smaller details of the particle shapes and surface can also be introduced by changing the positions of basis points. Each of the faces and vertices of the material target can be modified independently to add finer and specific details. The advantage of manual mode is that final target could be shaped into any nonspherical and highly irregular geometry. Along with the shape modifiers other material properties like size and aspect ratio can be easily set to match the realistic particle in laboratory samples. As per the requirements of dipole conversion softwares, the generated object is arranged finally in a triangular mesh (a specimen target is shown in Figure 3.3).

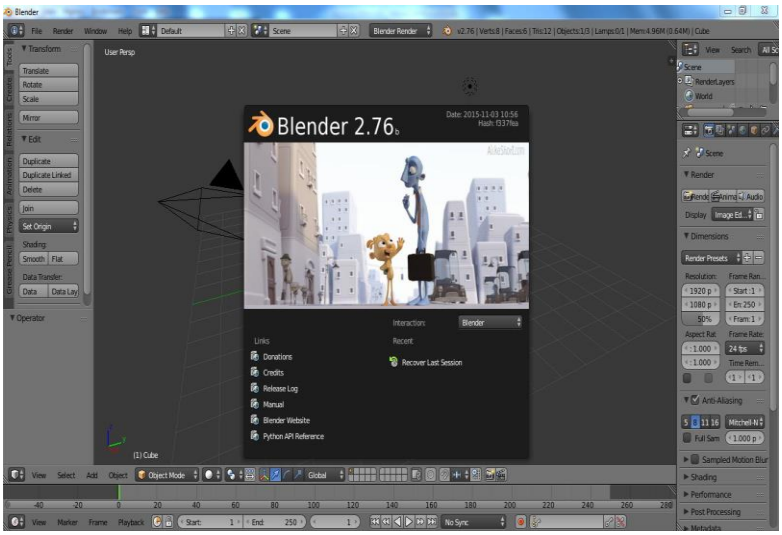

Figure 3.1 Graphical User Interface of Blender - geometry generation software.

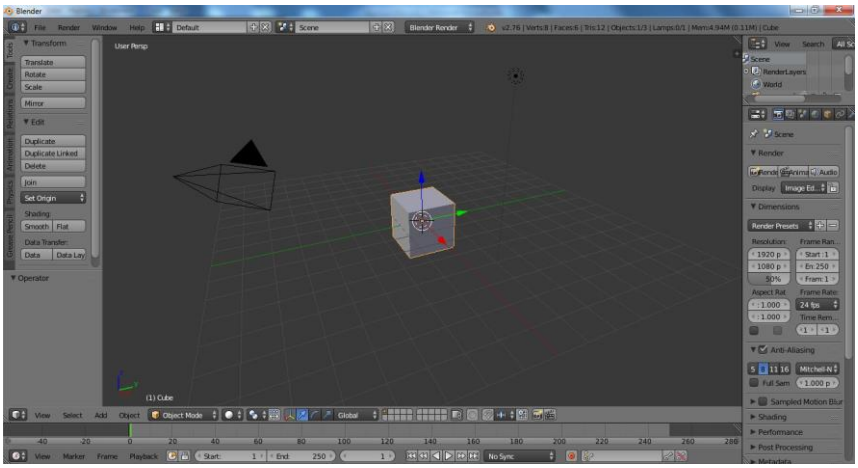

Figure 3.2 A primitive basis shape in Blender.

Figure 3.3 Specimen shapes generated using *Blender 2.76b*.

3.2.2 DDSCATConvert

The second step involves conversion of the generated target geometries into dipole arrays. DDSCATConvert is a software availabe in the public domain nanohub.org which facilitates replacement of the volumetric target geometries by representative polarizable points or dipoles. At first the shape generated in Blender is loaded into the Graphical User Interface (GUI) of DDSCATConvert in a wavefront.obj format. The requirement is that the input object must be in the form of a triangular mesh. Dipoles can be used to populate any arbitrary shape that is introduced as an object file with locations of all the virtual points that formed the particular geometry. The algorithm of this software uses the point in a polyhedron method where a numerical algorithm first checks for a point within a volumetric box. After that, a dipole is assigned to that particular position or space coordinate. The produced target in the form of a dipole array can now be directly used by the DDA code for light scattering calculations. The final output of this software is a shape file with 3D cordinates of all the point dipoles that populate the whole target volume. There are options available for setting the total number of dipoles for the conversion along with specifying

the number of different materials that can be available in a particular target, along with facilities for specifying material dielectric properties for the different shapes present in the target sample.

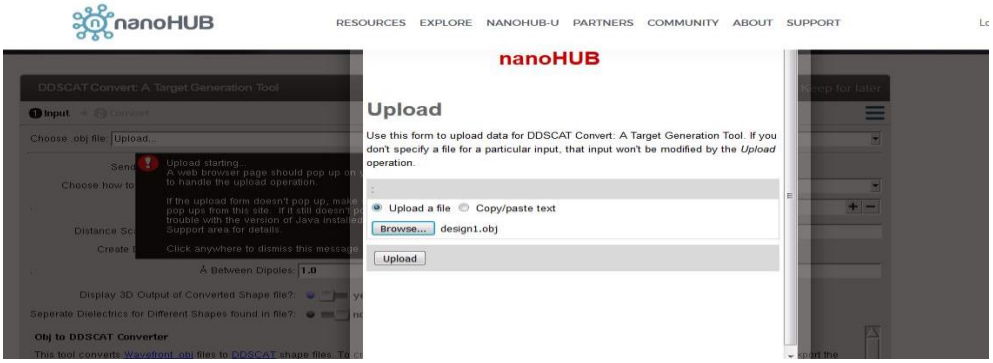

Figure 3.4 GUI of DDSCAT Convert for shape file

Figure 3.4 shows the Graphical User Interface of DDSCATCoonverter online html tool which provides the user an option to upload the target directly as an object file.

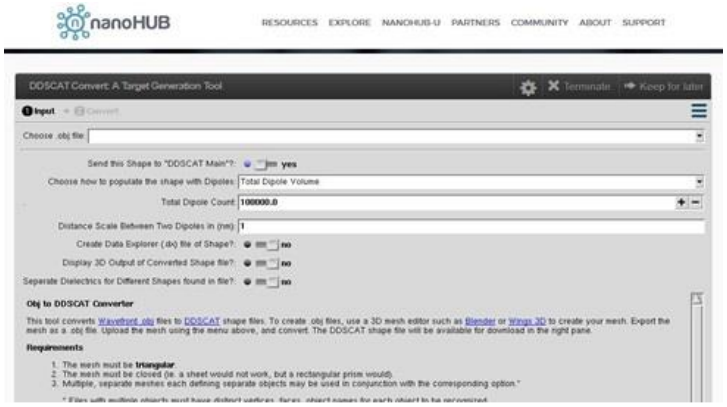

Figure 3.5 The input parameters of DDSCATConvert.

Figure 3.5 shows a screenshot of the input parameters for initiating the conversion of geomteries into dipole arrays.

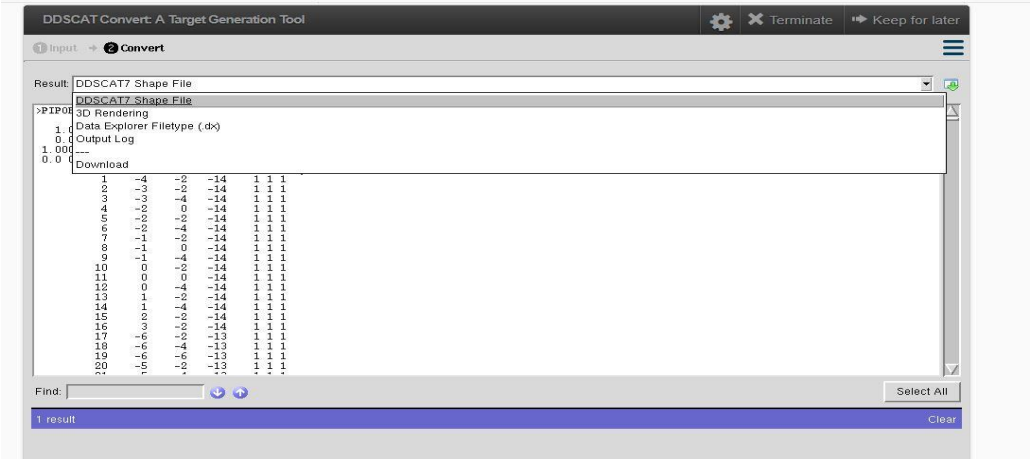

Figure 3.6 3D coordinates of dipoles in the converted target.

In the final stage of target conversion procedure, the software offers a option to save the generated output as shape and image files. Figure 3.6 shows a screen capture of the different files which can be directly downloaded from the remote server window of the website nanohub.org. Figure 3.7 shows the final generated target geometry. The whole process can be carried out online either in a html or java based window system. The conversion time is a function of the number of dipoles and also the number of different shapes in the target volume.

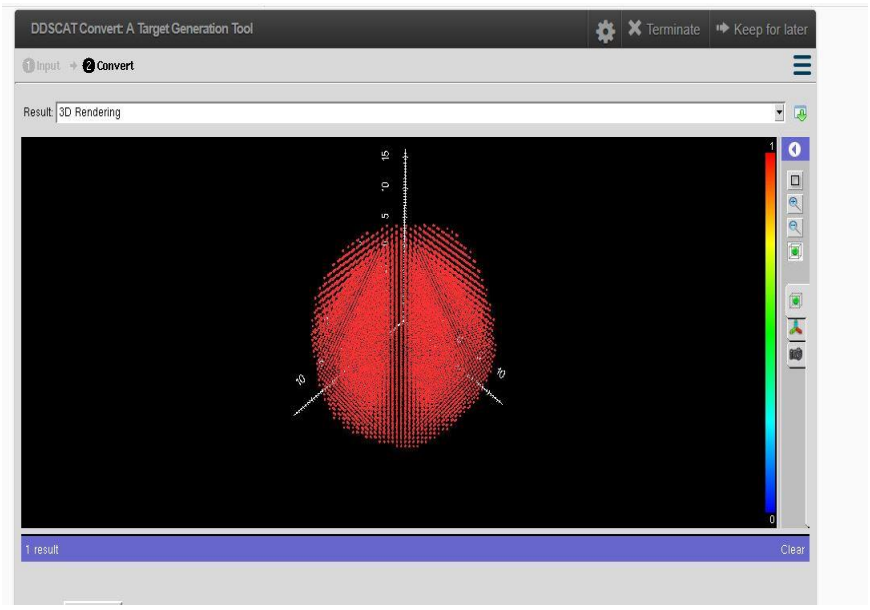

Figure 3.7 3D representation of target in reference coordinate system.

3.2.3 ParaView

ParaView is a freely available software which facilitates visualization and processing of complex data sets. This software is incorporated in our computational technique to visualize the target geometries developed using Blender3D and converted to dipole arrays in DDSCATConvert. The produced shape file can be introduced into the ParaView interface and a 3D rendered clear representation of the volumetric geometry of the shape is obtained as the final output. Its advantage is that the dipole arrays can be located in distinct and high resolution images in fine details. In advanced calculations the positions and vacant spaces can also be obtained. A target in dipole representation is shown in Figure 3.8.

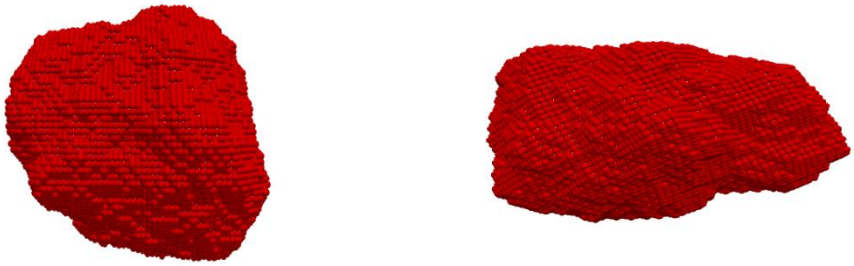

Figure 3.8 3D rendered representation of dipole arrays for specimen targets.

3.2.4 DDSCAT: Advantages and Limitations

The most advantageous feature of this FORTRAN90 code is that it can identify any user introduced arbitrary random Gaussian and irregular shapes and calculate their optical and radiative properties. The basic idea of DDA and DDSCAT are discussed in details in Chapter 1 (1.3.2.3. Discrete Dipole Approximation (DDA) and 1.3.3.2. DDSCAT code) and the theory of DDA along with mathematical formalism and calculations are provided in Chapter 2 (2.3. Theory and mathematical formalism of Discrete Dipole Approximation (DDA)).

The input parameters for DDA that requires to be specified by the user are,

1. Incident wavelength.
2. Refractive index, particle size, user defined shape file, particle size distribution.
3. Number of iterations for the computations and number of different dielectric materials.
4. Number of scattering and polarization directions to be considered for calculation.
5. Number of orientations and the scattering parameters to be calculated.

ddscat.par

```
' ========== Parameter file for v7.3 ==================='
'**** Preliminaries ****'
'NOTORQ' = CMTORQ*6 (DOTORQ, NOTORQ) -- either do or skip torque calculations
'PBCGS2' = CMDSOL*6 (PBCGS2, PBCGST, GPBICG, QMRCCG, PETRKP) -- CCG method
'GPFAFT' = CMETHD*6 (GPFAFT, FFTMKL) -- FFT method
'GKDLDR' = CALPHA*6 (GKDLDR, LATTDR, FLTRCD) -- DDA method
'NOTBIN' = CBINFLAG (NOTBIN, ORIBIN, ALLBIN)
'**** Initial Memory Allocation ****'
500 500 500 = dimensioning allowance for target generation
'**** Target Geometry and Composition ****'
'FROM_FILE' = CSHAPE*9 shape directive
no SHPAR parameters needed
1         = NCOMP = number of dielectric materials
'../diel/fayalite' = file with refractive index 1
'**** Additional Nearfield calculation? ****'
0 = NRFLD (=0 to skip nearfield calc., =1 to calculate nearfield E)
0.0 0.0 0.0 0.0 0.0 0.0 (fract. extens. of calc. vol. in -x,+x,-y,+y,-z,+z)
'**** Error Tolerance ****'
1.00e-5 = TOL = MAX ALLOWED (NORM OF |G>=AC|E>-ACA|X>)/(NORM OF AC|E>)
'**** Maximum number of iterations ****'
500      = MXITER
'**** Integration cutoff parameter for PBC calculations ****'
1.00e-2 = GAMMA (1e-2 is normal, 3e-3 for greater accuracy)
'**** Angular resolution for calculation of <cos>, etc. ****'
0.1      = ETASCA (number of angles is proportional to [(3+x)/ETASCA]^2 )
'**** Vacuum wavelengths (micron) ****'
0.5435 0.5435 1 'INV' = wavelengths (first,last,how many,how=LIN,INV,LOG)
'**** Refractive index of ambient medium'
1.0000 = NAMBIENT
'**** Effective Radii (micron) **** '
2.0 2.0 1 'LIN' = eff. radii (first, last, how many, how=LIN,INV,LOG)
'**** Define Incident Polarizations ****'
(0,0) (1.,0.) (0.,0.) = Polarization state e01 (k along x axis)
2 = IORTH  (=1 to do only pol. state e01; =2 to also do orth. pol. state)
'**** Specify which output files to write ****'
1 = IWRKSC (=0 to suppress, =1 to write ".sca" file for each target orient.
```

Figure 3.9 DDSCAT input parameter file part 1.

```
'**** Specify Target Rotations ****'
0.    0.   1  = BETAMI, BETAMX, NBETA  (beta=rotation around a1)
0.    0.   1  = THETMI, THETMX, NTHETA (theta=angle between a1 and k)
0.    0.   1  = PHIMIN, PHIMAX, NPHI (phi=rotation angle of a1 around k)
'**** Specify first IWAV, IRAD, IORI (normally 0 0 0) ****'
0   0   0    = first IWAV, first IRAD, first IORI (0 0 0 to begin fresh)
'**** Select Elements of S_ij Matrix to Print ****'
6       = NSMELTS = number of elements of S_ij to print (not more than 9)
11 12 21 22 31 41       = indices ij of elements to print
'**** Specify Scattered Directions ****'
'LFRAME' = CMDFRM (LFRAME, TFRAME for Lab Frame or Target Frame)
1 = NPLANES = number of scattering planes
0.  0. 180. 5 = phi, theta_min, theta_max (deg) for plane A
90. 0. 180. 5 = phi, theta_min, theta_max (deg) for plane B
```

Figure 3.10 DDSCAT input

Figure 3.9 and 3.10 shows the input parameter files which needs to be modified before carrying out the computation. All the input parameters must be keyed in manually in the parameter file which must be executed along with the main executable FORTRAN file named “ddscat”. After specifying the values of all the variables in the code, the shape file must be introduced in a DDSCAT compatible file format. Figure 3.11 shows the screen capture of the shape file with location of each and every dipole along with its dielectric properties.

```
 PIPOBJ: point-in-polyhedron: NBX, NBY, NBZ=  57 107  50
     102472 = NAT
   1.0000   0.0000   0.0000 = A_1 vector
   0.0000   1.0000   0.0000 = A_2 vector
 1.000000 1.000000 1.000000 = lattice spacings (d_x,d_y,d_z)/d
 0.0 0.0 0.0
         JA    IX    IY    IZ   ICOMP(x,y,z)
          1   -11     3   -24    1 1 1
          2   -10     3   -24    1 1 1
          3   -12    10   -24    1 1 1
          4    -9     3   -24    1 1 1
          5   -11    10   -24    1 1 1
          6   -10    10   -24    1 1 1
          7    -9    10   -24    1 1 1
          8    -8    10   -24    1 1 1
          9    -7    -4   -24    1 1 1
         10    -7    10   -24    1 1 1
         11    -6    10   -24    1 1 1
         12    -5    10   -24    1 1 1
         13    -4    10   -24    1 1 1
         14    -3    10   -24    1 1 1
         15    -2    10   -24    1 1 1
         16    -1    10   -24    1 1 1
         17     0    10   -24    1 1 1
         18   -13     3   -23    1 1 1
         19   -12     3   -23    1 1 1
         20   -13    10   -23    1 1 1
         21   -12    10   -23    1 1 1
         22   -11     3   -23    1 1 1
         23   -11    10   -23    1 1 1
         24   -10    10   -23    1 1 1
         25   -10     3   -23    1 1 1
         26    -9    10   -23    1 1 1
         27    -8    10   -23    1 1 1
         28    -7    10   -23    1 1 1
         29    -6    10   -23    1 1 1
```

Figure 3.11 Shape file after conversion with DDSCATConvert.

After modifying the input parameters and loading the shape file with dipole locations, the main code of DDA is executed. The conversion time depends on particle size, number of dipoles and iterations required to perform the calculations of cross sections and scattering parameters. The number of directions selected for orientational averaging further lengthen the time required for completion of the computational procedure. The computations in this entire thesis work are carried out in a workstation with 3.6 GHz core i7 processor equipped with 6 GB Random Access Memory (RAM). The average timing for computations with different samples varies from a time range of 12 hours to 72 hours respectively along with the time required for size and shape averaging. Once the computation completes, all the output files are automatically saved in folders specified by the user, which can be later accessed for data processing and graph plotting. Figure 3.12 and 3.13 shows the output file containing the scattering, absorption and extinction efficiencies ($Q_{sca}, Q_{abs}, Q_{ext}$ respectively), single scattering albedo (a), asymmetry parameter (g) and all the theoretical Mueller matrix elements (F_{ij}) including the polarization (P).

w000r000.avg ×

```
 DDSCAT --- DDSCAT 7.3.0 [13.05.03]
 TARGET --->PIPOBJ: point-in-polyhedron: NBX, NBY, NBZ =  43  43  51
 GKDLDR --- DDA method
 PBCGS2 --- CCG method
 FROM_FILE --- shape
   29675     = NAT0 = number of dipoles
  0.05206740 = d/aeff for this target [d=dipole spacing]
    0.052067 = d (physical units)
  AEFF=      1.000000 = effective radius (physical units)
  WAVE=      0.543500 = wavelength (in vacuo, physical units)
K*AEFF=     11.560598 = 2*pi*aeff/lambda
NAMBIENT=    1.000000 = refractive index of ambient medium
n= ( 2.7312 ,  1.5608),  eps.= (  5.0233 ,  8.5260)  |m|kd=  1.8935 for subs. 1
   TOL= 1.000E-05 = error tolerance for CCG method
( 1.00000  0.00000  0.00000 ) = target axis A1 in Target Frame
( 0.00000  1.00000  0.00000 ) = target axis A2 in Target Frame
  NAVG=  5832 = (theta,phi) values used in comp. of Qsca,g
( 0.60193  0.00000  0.00000 ) = k vector (latt. units) in Lab Frame
( 0.00000, 0.00000 )( 1.00000, 0.00000 )( 0.00000, 0.00000 )=inc.pol.vec. 1 in LF
( 0.00000, 0.00000 )(-0.00000, 0.00000 )( 1.00000,-0.00000 )=inc.pol.vec. 2 in LF
   0.000   0.000 = beta_min, beta_max ;  NBETA = 1
   0.000   0.000 = theta_min, theta_max; NTHETA= 1
   0.000   0.000 = phi_min, phi_max   ;   NPHI = 1

 0.5000 = ETASCA = param. controlling # of scatt. dirs used to calculate <cos> etc.
 Results averaged over    1 target orientations
                      and    2 incident polarizations
          Qext        Qabs        Qsca      g(1)=<cos>  <cos^2>     Qbk       Qpha
 JO=1:  3.3327E+00  1.4826E+00  1.8502E+00  8.6824E-01 8.7289E-01 8.0515E-04 -1.4048E-01
 JO=2:  3.3346E+00  1.4065E+00  1.9281E+00  8.5000E-01 8.6714E-01 1.2050E-02 -1.6364E-01
 mean:  3.3337E+00  1.4445E+00  1.8892E+00  8.5893E-01 8.6714E-01 6.4275E-03 -1.5206E-01
 Qpol= -1.9379E-03                                                dQpha=  2.3165E-02
        Qsca*g(1)   Qsca*g(2)   Qsca*g(3)   iter  mxiter  Nsca
 JO=1:  1.6064E+00 -3.3261E-02  2.2168E-02    101    300   5832
 JO=2:  1.6389E+00  2.7748E-02 -3.6203E-03    101    300   5832
 mean:  1.6227E+00 -2.7566E-03  9.2741E-03
```

Figure 3.12 The main output file of DDSCAT part 1.

Mueller matrix elements for selected scattering directions in Lab Frame

theta	phi	Pol.	S_11	S_12	S_21	S_22	S_31	S_41
0.00	0.00	0.01171	1.2511E+04	-2.3320E+01	-2.254E+01	1.251E+04	-1.448E+02	-5.266E+01
5.00	0.00	0.02581	7.5240E+03	-1.9444E+02	-1.936E+02	7.522E+03	-1.569E+01	-4.405E+01
10.00	0.00	0.12510	1.5845E+03	-1.9684E+02	-1.963E+02	1.583E+03	2.758E+01	-2.378E+01
15.00	0.00	0.61236	7.9568E+01	-4.7644E+01	-4.746E+01	7.764E+01	-1.102E+01	-4.143E+00
20.00	0.00	0.24694	2.8009E+02	-6.3409E+01	-6.323E+01	2.786E+02	-2.803E+01	4.290E+00
25.00	0.00	0.56694	1.2129E+02	-6.7911E+01	-6.761E+01	1.206E+02	-1.255E+01	3.841E+00
30.00	0.00	0.36759	7.1787E+01	-2.6590E+01	-2.633E+01	7.147E+01	-1.753E+00	4.177E+00
35.00	0.00	0.38885	9.3332E+01	-3.6443E+01	-3.627E+01	9.316E+01	1.314E+00	4.494E+00
40.00	0.00	0.76955	4.1951E+01	-3.2317E+01	-3.220E+01	4.179E+01	2.345E+00	2.807E+00
45.00	0.00	0.59777	3.1469E+01	-1.8716E+01	-1.869E+01	3.126E+01	2.150E+00	1.732E+00
50.00	0.00	0.65632	3.1845E+01	-2.0730E+01	-2.079E+01	3.160E+01	2.129E+00	1.499E+00
55.00	0.00	0.92333	2.0349E+01	-1.8577E+01	-1.871E+01	2.004E+01	1.701E+00	8.213E-01
60.00	0.00	0.89776	2.1441E+01	-1.9000E+01	-1.921E+01	2.103E+01	1.254E+00	1.788E-01
65.00	0.00	0.95480	2.4768E+01	-2.3385E+01	-2.361E+01	2.440E+01	1.286E+00	2.264E-01
70.00	0.00	0.97412	2.4335E+01	-2.3519E+01	-2.364E+01	2.401E+01	1.778E+00	6.223E-01
75.00	0.00	0.94293	2.3083E+01	-2.1611E+01	-2.162E+01	2.269E+01	2.513E+00	9.856E-02
80.00	0.00	0.97467	1.9942E+01	-1.9292E+01	-1.935E+01	1.959E+01	1.878E+00	-1.480E+00
85.00	0.00	0.98051	1.9065E+01	-1.8582E+01	-1.869E+01	1.886E+01	-2.784E-01	-1.481E+00
90.00	0.00	0.98144	2.2954E+01	-2.2449E+01	-2.249E+01	2.277E+01	-1.270E+00	1.003E+00
95.00	0.00	0.98905	2.8610E+01	-2.8244E+01	-2.830E+01	2.828E+01	-2.001E-01	2.998E+00
100.00	0.00	0.96818	3.1351E+01	-2.9951E+01	-3.035E+01	3.074E+01	4.492E-01	2.270E+00
105.00	0.00	0.90768	2.6931E+01	-2.3603E+01	-2.444E+01	2.604E+01	-1.633E-01	-3.365E-01
110.00	0.00	0.73231	1.8262E+01	-1.2601E+01	-1.337E+01	1.749E+01	3.399E-01	-2.111E+00

Figure 3.13: The main output file of DDSCAT part 2.

It is already discussed that for accurate numerical results the DDA condition must be fulfilled. Which requires $|m|kd \leq 1$. So it is necessary to ensure the incident wavelength, particle sizes and the number of dipoles must not exceed this limit. An important factor can be defined as the size parameter ' x ' which is critical in validating any DDA computation.

$$x = 2\pi r_{eff} / \lambda \leq 25 \qquad \textbf{3.1}$$

where ' r_{eff} ' is the effective radius of the target material.

But there are limits to the real and imaginary refractive index values that can be given for computation. To minimize errors and ensure computational accuracy, the interdipole separations *d* must be kept to a low value while carrying out the computations. Also practical limitations due to the computer processor's capability and Random Access Memory (RAM) availability occurs which requires that $N \leq 10^6$. The limitations on size parameter, $|m|kd$ and the value of N makes it evident that the ratio of target size to wavelength must be kept at a critical value at the beginning of a computation to satisfy all necessary criterions.

The applicability of DDA to targets having a wide range of complex refractive values and size distributions have been reviewed by a number of research groups and their reports of the advantages and disadvantages of the code are available.

Several research groups conducting independent research works using DDA arrived at the conclusion that the cross section are relatively accurate if the number of dipoles considered exceeds a minimum value $N > 10^4$ [1-3].

Another comparative study with Mie theory and T-matrix shows that despite the limitations regarding the memory requirements this technique is most appropriate for particles with arbitrary and irregular geometries [4].

It is extremely difficult to find out the accuracy and advantages of volume integral techniques like DDA while compared to other techniques. That makes this technique powerful and effective but unpredictable [5].

Keeping aside mathematical and practical limitations, DDA is the only numerical technique available which is not restricted by shape and geometry of the scattering particle. [6-8]. With the increasing speeds of powerful processors and high RAM availabilities the earlier DDA permissible limit of maximum number of dipoles (10^6) is now extended to much larger values further decreasing the value of interdipole separations 'd'[9]. Also it is proved that relatively accurate measurements of scattering matrix elements is possible if the dipoles are arranged in a cubic lattice [10].

Most accurate calculations performed by DDA is of the values of F_{11}(the most important scattering parameter for unpolarised incident light). The accuracy is effected mainly by the lattice dispersion relations in the large size parameters range.

The speed and accuracy test of DDA, Extended Boundary Condition Method (EBCM) and Finite Difference Time Domain (FDTD) method shows that DDA is faster

and accurate enough to be a reliable tool of computation for moderate size parameter and refractive indices [5, 11, 12].

3.2.5 Size and shape averaging of realistic samples

In realistic modelling and simulation studies of light scattering as reported in this thesis, the particle size distribution and shapes considered for theoretical calculations are based on the samples either synthesized in the laboratory or acquired from chemical suppliers. A particular area or volume element in a Scanning Electron Micrograph (SEM) image is first identified and all the particle sizes are measured using software tools like ImageJ. After that the most common shapes that constitute the particulate matter sample are considered for target generation.

The particle surface area or the total volume is first measured using the maximum length of the irregular particle as reference with the surface or volume equivalent radius. This radius is used as the effective size of the particulate sample to carry out the computations. As it is not possible to directly measure the volume or surface of a highly irregular particle, it requires to assume the particle to be in the form of either a cuboid or a prolate ellipsoid.

Some of the important parameters that require to be defined for particle size distribution measurements are aspect ratio, volume equivalent sphere radius r_V , and surface equivalent sphere radius (r_S) [13].

where Aspect ratio = (l / b)

l and b are length and breadth of the particle,

and volume of a cuboid and an ellipsoid is given by,

Volume (V) = $\frac{4}{3}\pi abc$ **3.2**

Or, Volume = $a \times b \times c$ **3.3**

Where a, b, and c are length, breadth and thickness of a cuboid and lengths of the three axes for a prolate ellipsoid.

Volume equivalent sphere radius (r_v): Now the volume equivalent sphere radius can be defined as the radius of a sphere with volume equal to the particle.

The volume of a sphere is given by,

$$V = \frac{4}{3}\pi r^3$$

And the volume equivalent sphere radius can be written as,

$$r_v = \left(3V_{particle} \Big/ 4\pi\right)^{1/3} \qquad \textbf{3.4}$$

Surface equivalent sphere radius (r_s): Surface equivalent radius of a particle is the radius of a sphere with the same surface area as that of the particle.

Surface equivalent radius can be written as,

$$r_s = \left(3S_{particle} \Big/ 2\pi\right)^{1/2} \qquad \textbf{3.5}$$

3.2.5.1 MATLAB© code for Post processing

Most of naturally occurring small particles have highly indistinguishable size, shape or random direction of orientation. While calculating the radiation cross sections and light scattering parameters, it is assumed that for a system of randomly oriented arbitrary shaped and sized particles the radiative properties are similar to a system of volume equivalent sphere averaged over a particular size range [14, 15]. However, extensive studies have revealed that these assumptions are not applicable to all practical cases [16]. For realistic modelling of interstellar dust analogues it is required to consider enormous variations in shapes and sizes of those highly irregular particles [17-21] more accurately. In order to simulate the properties of dust analogue samples, aided by laboratory experiments, a post processing MATLAB© code was developed which can compute the scattering parameters and efficiencies for a shape and size dispersed target. This code takes the files generated by DDSCAT for each shape and size and performs averaging for the target properties. The MATLAB© post processing tool which incorporates normal, lognormal and gamma size distribution functions, is used to generate size and shape averaged plots of computational values of Mueller Matrix elements. Studies have shown that the natural systems of polydisperse particles can be well represented by size distributions functions such as gamma, normal, lognormal etc. [9, 22, 23, 24]. But realistic results are arrived at only if the linear dimension of the scattering volume is smaller than the distance between the origin and the detector.

It has been reported that the experimentally measured size distribution of water droplets can be reproduced with gamma distribution [22, 25, 26]. The gamma distribution is given by,

$$n(r) = ar^{\alpha} \exp(-br) \qquad \textbf{3.6}$$

where $a = N\dfrac{b^{\alpha+1}}{\Gamma(\alpha+1)}$ and $b = \dfrac{\alpha}{r_m}$

'r' is the particle radius, r_m is the modal radius, a is a constant, Γ is the gamma function and α is a parameter which characterizes the width of the function.

The normal and lognormal size distribution functions can represent aerosol size distributions [9, 24, 27, 28, 29].

The normal size distribution is given by [30],

$$n(r) = \frac{1}{(2\pi)^{1/2}\sigma_g} \exp\left[-\frac{(r-r_g)^2}{2\sigma_g{}^2}\right] \qquad \textbf{3.7}$$

Also lognormal function is written as [31],

$$n(r) = \frac{N}{(2\pi)^{1/2} r \ln(\sigma_g)} \exp\left[-\frac{(\ln r - \ln r_g)^2}{2\ln^2(\sigma_g)}\right] \qquad \textbf{3.8}$$

in the above expression r is the particle radius, $n(r)$ is the number of particles with radius r, 'σ_g' is the standard deviation of the size distribution, r_g is modal radius, N is the number concentration with modal radius.

3.3 Experimental setup for light scattering studies

The most important part of a light scattering setup is the measurement of light intensity precisely for the whole scattering angle range 0° to 180° using suitable combinations of lasers, polarizers and photodetectors. The parameter that is measured other than intensity is the polarization of scattered light. The detection of scattered signal as angle dependent function and subsequent development of relations to the Muller matrix elements constitutes the major part of data analysis.

3.3.1 Measurable quantities of a light scattering event

For a quasi-monochromatic plane wave the wave equation for the electric field is,

$$E(r,t) = E_0 e^{-i(kr-wt)} \quad \textbf{3.9}$$

The scattered intensity can be related to the incident wave for a multi particle system as [32],

$$\mathbf{I_S} = \frac{F(\theta,\phi)}{k^2 d^2}\mathbf{I_i} \quad \textbf{3.10}$$

where $F(\theta,\phi) = \sum_N F(\theta,\phi)$ and N is the total number of particles.

And also from the definition of the Stokes vector we have,

$$\begin{pmatrix} I_S \\ Q_S \\ U_S \\ V_S \end{pmatrix} = \frac{1}{k^2 d^2} F \begin{pmatrix} I_i \\ Q_i \\ U_i \\ V_i \end{pmatrix} \quad \textbf{3.11}$$

where *F* is the Mueller matrix. Now for unpolarized incident light we can directly write the scattered stokes vectors as [32, 33],

$$I_S = F_{11}, Q_S = F_{21}, U_S = F_{31}, V_S = F_{41} \quad \textbf{3.12}$$

But as for unpolarized light the values of Q_S, U_S and V_S are zero, we can also write $F = F_{11}$ [Using equation 3.11 and 3.12].

And polarization $P = \dfrac{(F_{21}^2 + F_{31}^2)^{1/2}}{F_{11}}$

The physical significance of F_{11} is that it represents the total intensity of scattered light at specific scattering angles and the degree of linear polarization defines the extent of linear polarization induced by the scatterer in the incident beam.

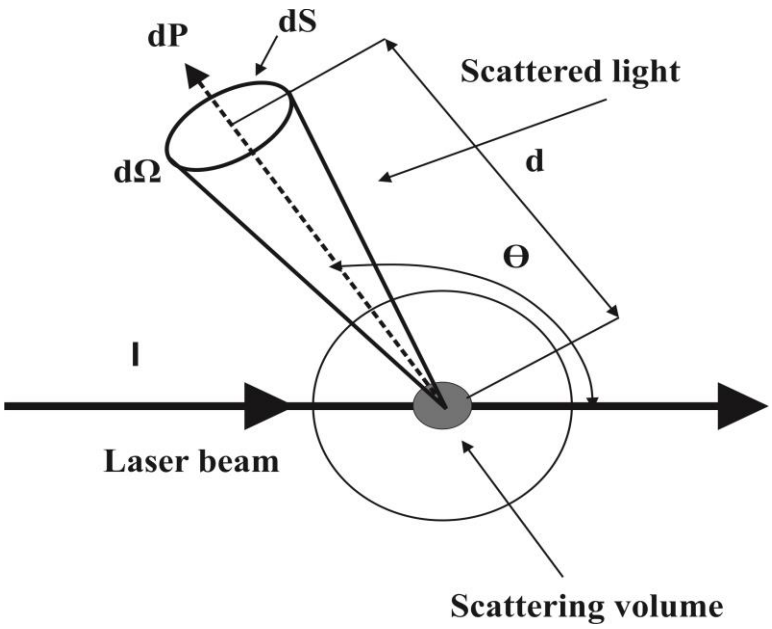

Figure 3.14 Scattered beam and the detector.

Figure 3.14 shows light scattered from a system of particles in a small volume of length *l.* The incident beam I of total irradiance (P_i) illuminates this volume element in the scattering plane. This scattering volume radiates power dP along the scattering direction θ per unit solid angle dΩ subtended per unit area dS. dΩ is the soild angle subtended by the detector placed at a distance D from the scattering volume, where $d\Omega = \frac{dS}{D^2}$.

All mathematical treatments are based on unpolarized incident light, as applicable to this study.

Considering light scattered from a volume element an expression for the volume scattering function can be written as [34, 35],

$$\beta(\theta,\phi) = \frac{dR(\theta,\phi)}{P_i dv} \qquad \textbf{3.13}$$

Here $dR(\phi,\theta)$ is a part of the scattered intensity along an arbitrary direction specified by scattering angle θ and azimuthal angle ϕ, 'dv' is a small volume element along the direction of scattering and P_i is the total irradiance of the incident light. Thus the volume scattering function may be defined as the scattered light intensity per unit irradiance of the incident light per unit volume.

Again,

$$\beta(\theta) = \frac{dR(\theta)}{P_i dv} \qquad \textbf{3.14}$$

For spatially symmetric particles the volume scattering function $\beta(\theta)$ is of the simple form as in equation 3.14 depending only on the scattering angle θ [29, 36], and is a measurable quantity using practical instruments.

For practical applications e.g. measurement of light scattering properties with laboratory experiments it is convenient to define a parameter phase function ($f(\theta)$) which is equivalent to $F_{11}(\theta)$ of the Mueller matrix.

Physically it represents the size and shape averaged scattering measurements of a system of randomly oriented particles.

Or,

$$f(\theta) = \frac{\beta(\theta)}{s} \qquad \textbf{3.15}$$

where *s* is the scattering coefficient and is defined as the average over scattering function for a full solid angle.

$$s = 2\pi \int_0^{\pi} \beta(\theta) \sin\theta \, d\theta \qquad \textbf{3.16}$$

Experimental measurements of the elements $F_{ij}(\theta)$ of the Mueller matrix or scattering matrix are done by using different arrangements of polarizers and analyzers which are placed in front of the incident and scattered beam. In this thesis work $F_{11}(\theta)$ or phase function and polarization or the degree of linear polarization $P(\theta)$ are measured. The phase function can be directly determined by measuring the scattered light intensity as functions of scattering angle for unpolarized incident light.

Further, phase function can be written as,

$$F_{11}(\theta) = I_S(\theta) \qquad \textbf{3.17}$$

where $I_S(\theta)$ is the total intensity of scattered light at scattering angle θ when the incident light is unpolarized.

Again for unpolarised incident light, polarization can be defined as the mathematical ratio of the second and first element of the Mueller matrix i.e. $F_{12}(\theta)$ and $F_{11}(\theta)$ are provided $F_{13}(\theta) = F_{14}(\theta) = 0$.

For a single particle in a randomly oriented systems the scattered radiance is given by the equation [37, 38],

$$I(\theta) = \sigma R_P Q_S \frac{F_A(\theta)}{4\pi} \quad \textbf{3.18}$$

Where ' R_P ' is the total irradiance of the incident unpolarized light. ' σ ' is the average cross sectional area of the particle over all orientation directions, $F_A(\theta)$ is scattering function, Q_S is the scattering efficiency.

Now $I_\perp(\theta)$ and $I_\parallel(\theta)$ are the light intensities scattered parallel and perpendicular to the scattering plane such that,

$$I(\theta) = I_\perp(\theta) + I_\parallel(\theta) \quad \textbf{3.19.1}$$

And $$\Delta I(\theta) = I_\perp(\theta) - I_\parallel(\theta) \quad \textbf{3.19.2}$$

A factor called polarization can be defined using these two equations 3.19.1 and 3.19.2 [37],

$$P(\theta) = \frac{\Delta I(\theta)}{I(\theta)} \quad \textbf{3.20.1}$$

The degree of polarization can be practically determined as provided in the following expression [39 - 42],

$$P(\theta) = -\frac{\langle F_{12}(\theta)\rangle}{\langle F_{11}(\theta)\rangle} = \frac{I_\perp - I_\parallel}{I_\perp + I_\parallel} \text{ such that } |P(\theta)| \le 1 \quad \textbf{3.20.2}$$

3.3.2 The experimental setup for optical characterization

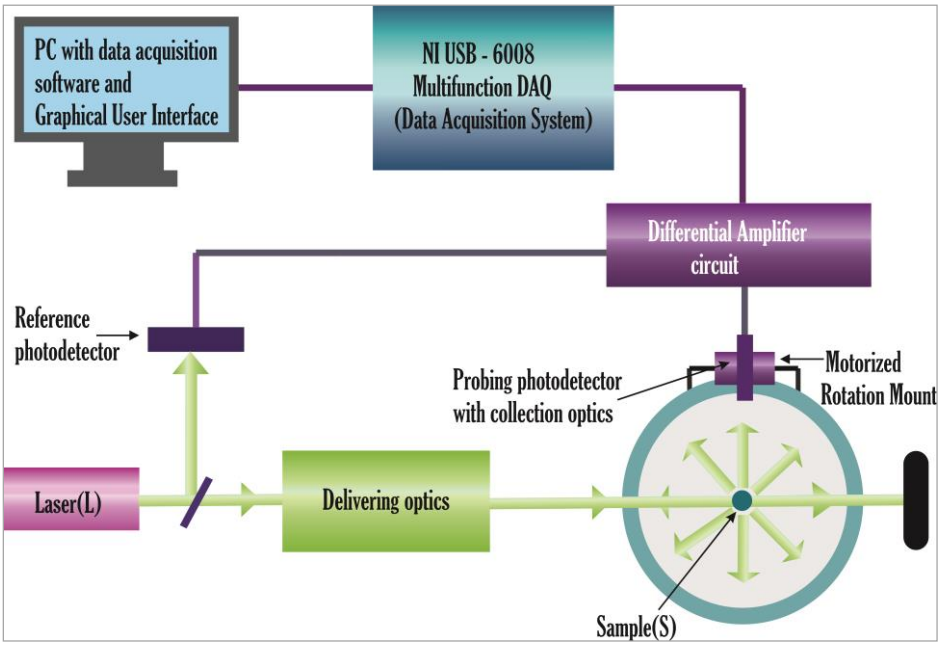

Figure 3.15 Schematic diagram of the light scattering setup.

An experimental setup was developed in the laboratory (Figure 3.15, 3.16 and 3.17) [43] to measure light scattering properties of particulate matter. It consists of a laser, a flexible particle sprayer system, photodetector and data acquisition system.

The setup can measure $F_{11}(\theta)$ and $-F_{12}(\theta)/F_{11}(\theta)$, over the scattering angle range from 10° to 170° in steps of 5°. It uses three lasers of wavelengths 543.5 nm, 594.5 nm and 632.8 nm alternately according to the requirement of the experiment. The photodetector was capable of rotating in the scattering plane using a stepper motor based rotor system. The light scattered from the samples was allowed to pass through a set of collection optics comprising of appropriate analyzers and were detected by the photodetector. The amplified signals were fed to the data acquisition system (DAQ NI USB – 6008) which was interfaced to the PC through the USB port for data storing and analysis.

The most important components of the fabricated light scattering setup has been explained in details along with the calibration tests and mathematical corrections incorporated into the measurement techniques. Figure 3.16 shows a photograph of the

experimental setup and figure 3.17 shows of a close up view of the main optical components.

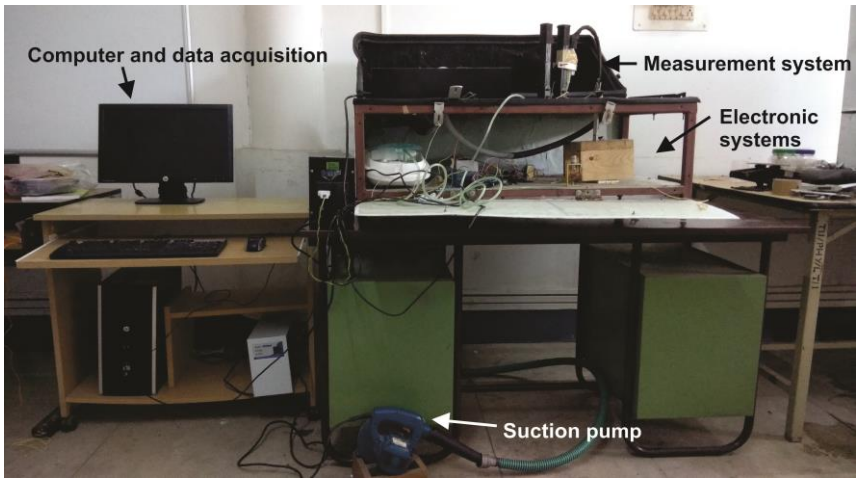

Figure 3.16 Photograph of the complete experimental setup.

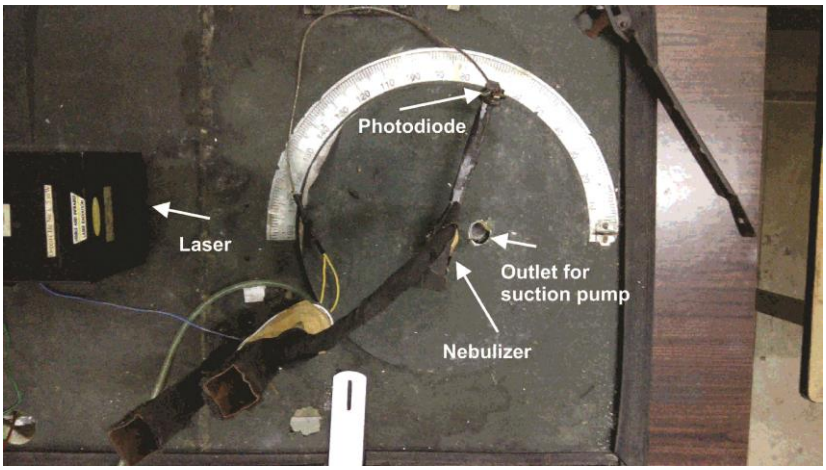

Figure 3.17 Top view of the experimental setup.

3.3.2.1 Lasers

Lasers are the basic requirements of a laboratory based optical characterization setup. A well-directed collimated and powerful light source is vital to illuminate the micron and submicron sized particle systems where the scattered light is relatively faint to detect. Ordinary light sources usually lack the power to produce a strong and detectable light scattering intensity pattern mainly in the visible range. In this setup three He-Ne lasers are used for investigations at different incident wavelengths in the range 300-700 nm.

The specifications of the three lasers are tabulated in Table 3.1.

Table 3.1 Specifications of the visible wavelength lasers

Sl. No.	Wavelength	Output Power
1	543.5 nm	5 mW
2	594.5 nm	5 mW
3	632.8 nm	2 mW

All the three lasers emit unpolarised light having beam diameters of approximately 1 mm [36].

For calibration purpose intensity of all the three lasers were measured at a distance of 250 mm (scattering centre) from the source and a micro positioner was used for the adjustments. The intensity profile of the laser beams are shown Figure 3.18.

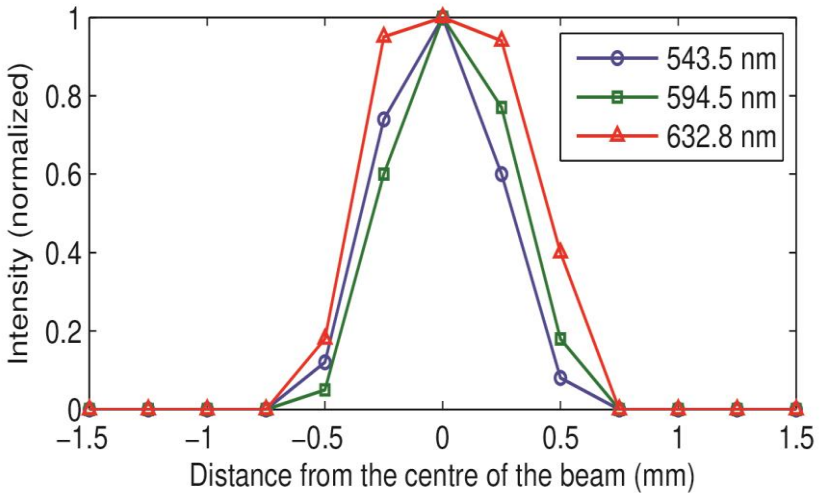

Figure 3.18 Profiles of the three laser wavelengths 543.5 nm, 594.5 nm and 632.8 nm respectively specified by symbols in the legend.

From the figure it is possible to observe that the profiles of the lasers with wavelength 543.5 nm and 594.5 nm are Gaussian in shape but for the 632.8 nm one it is flat top. The beam cross sections are measured to be approximately $0.5mm^2$ for all the three wavelengths.

3.3.2.2 Photodetector

Two highly sensitive UV – Visible photodiodes are used for detecting the light signals in the experimental setup. Each of the silicon photodiodes are suitable for sensing faint light signals scattered from the target. This type of high efficiency detectors are also suitable for precision photometry with supressed IR sensitivity.

The used photodiodes are S1227-16BR (Figure 3.19(a)) and BPW34 (Figure 3.19(b)).

a **b**

Figure 3.19 Photographs of (a) S1227-16BR and (b) BPW34.

The spectral response curves of the photodiodes are provided in Figure 3.20(a) and (b).

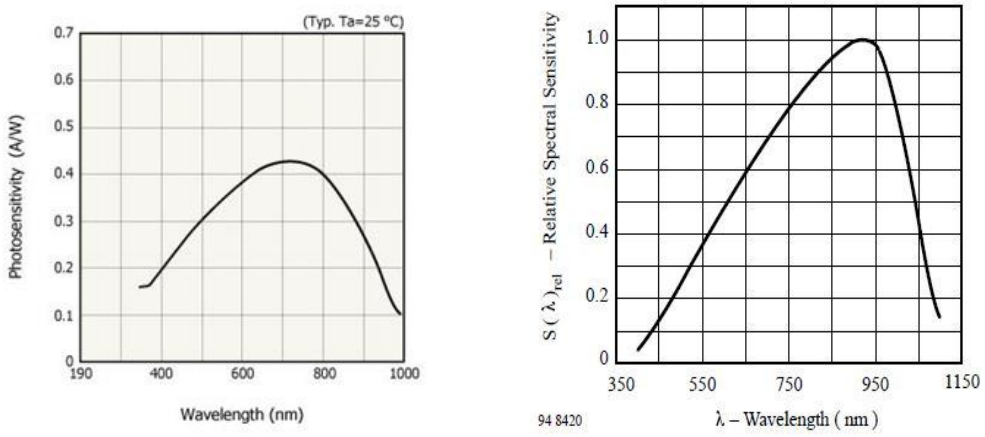

a **b**

Figure 3.20 Spectral response of (a) S1227-16BR and (b) BPW34.

Table 3.2 and 3.3 shows the specifications and special characteristics of **S1227-16BR** and **BPW34**.

Table 3.2 Specifications of the photodiode S1227-16BR

Photosensitive area	5.9 x 1 mm^2
Reverse voltage (max.)	5 V
Spectral response range	340 – 1000 nm
Peak sensitivity wavelength	700 nm
Rise time	0.5 µs
Terminal capacitance	170 pF

Table 3.3 Specifications of the photodiode BPW34

Photosensitive area	2.65 x 2.65 mm^2
Forward voltage	1.3 V
Spectral response range	400 – 1100 nm
Peak sensitivity wavelength	900 nm
Rise and fall time	20 ns
Terminal capacitance	72 pF

3.3.2.3 Particle sprayer system

The most important function of a particle sprayer system is to supply adequate number of particles per unit time in the light scattering experiment. The particles may be supplied in the form of continuous jet streams or periodic bursts synchronized with the detector's acquisition speed. The samples may be either solids (aerosols) or liquids (hydrosols). Adequate care must be taken to ensure minimum contamination by dust. There must be sufficient number of particles to produce strong detectable scattered signal while at the same time this number must not exceed density for single scattering only.

3.3.2.3.1 Aerosol sprayer system

A modified version of the particle sprayer system [36] based on an aerosol nebulizer as reported by Hovenier et al. is used in the setup [42]. The aerosol sprayer as shown in Figure 3.21 for producing a flow of particulate matter sample consists of a simple electric roller (R), a mechanical piston (P), sample holder (T), flow tube (B), nozzle (N) and a high tension spring coil (S). A metallic frame (H) provides mechanical support to the whole system. The powder sample is kept in the reservoir (a glass cuvette of 10mm diameter) for an entire scattering experiment. When the sample holder is full, the piston is pushed backwards with a force and is held by a high tension spring coil fitted to a mechanical support. A small amount of sample is carried over by a specially designed electric roller into the socket. An electric dc motor (12V) is used to rotate the roller at variable speeds. Once the roller takes away a reasonable amount of powder, the piston is pushed forward along with the sample. While in the downward motion, the roller socket feeds the sample into an air stream in the flow tube (B). The flow tube is a glass tube of 10 cm in length and 15 mm in diameter. Once the sample reaches the bottom end of the tube as aerosol particles, they are allowed

to pass through a nozzle (N) such that a fine jet stream of particles can be formed. The particles are carried away under force by a vacuum suction pump to ensure minimum dust contamination. Finally the aerosol jet comes within the scattering volume in the path of the laser beam. There is an arrangement (metallic tray) to collect the samples at the bottom of the sprayer system so that the sample can be reused.

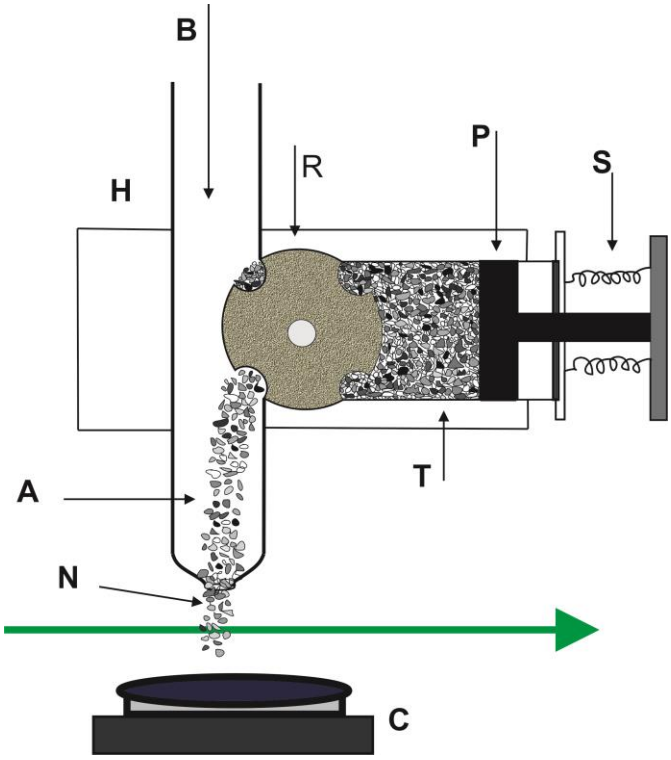

Figure 3.21 Schematic diagram of the Aerosol sprayer system**.**

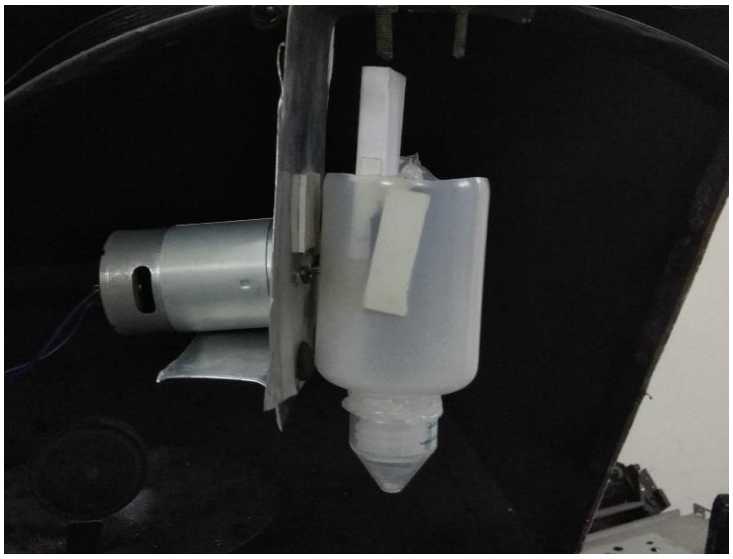

Figure 3.22 Photograph of the aerosol nebulizer.

3.3.2.3.2 Liquid particle sprayer system

To spray liquid particles into the scattering volume a liquid nebulizer or atomizer is used (Nu Life Nuneb Pro nebulizer). This is a type of instrument used in medication systems to deliver a fast supply of fine particles mainly to treat respiratory diseases. In nebulizers, a highly compressed jet of air or oxygen is allowed to pass through a liquid or suspension at extremely high velocities, which results in an aerosol of fine particles coming out through a nozzle. Figure 3.23 shows the nebulizer used in this work.

Figure 3.23 Photograph of the Nuneb pro nebulizer.

The specifications of the nebulizer is provided in Table 3.4.

Table 3.4 Specifications of the Nuneb pro nebulizer

Compressor	Piston
Pressure (Max.)	2.5 bar
Air flow (Min.)	8 LPM
Noise at 1 m	55 dba
Operating time	60 min. ON and 30 min. OFF
Particle size	0.5 – 5 microns
Power supply	215 – 240 V AC
Power consumption (Max.)	90 Watts
Size	$344mm \times 189mm \times 120mm$

3.3.2.4 Data acquisition system

For data acquisition and recording a NATIONAL INSTRUMENTS© manufactured dedicated Data acquisition system NI USB-6008 DAQ is used. This instrument offers real time data collection facility using the LabVIEW© based platform and an interactive plotter tool for fast and efficient data analysis and post processing. The signals collected by the photodiodes are directly fed into this DAQ system after proper amplification and analysed using the Graphical User Interface (GUI) to yield results and do comparative studies.

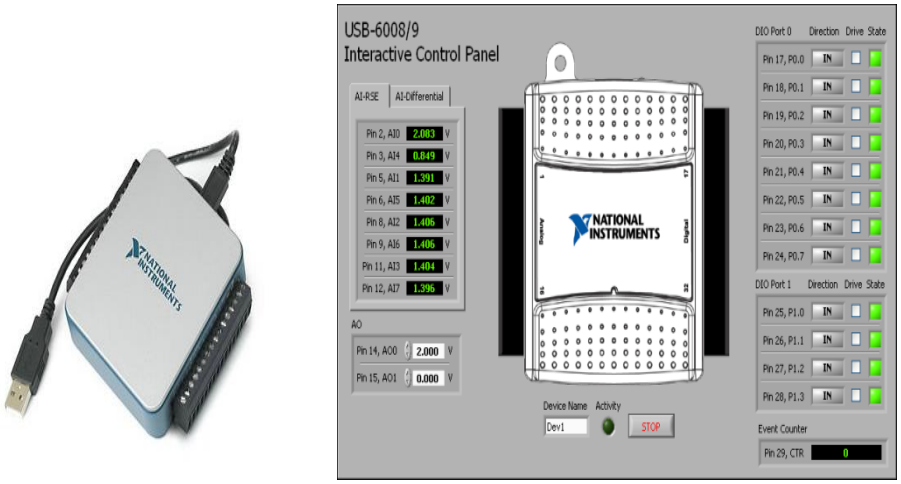

a **b**

Figure 3.24 (a) NI USB-6008 (b) Control panel

NI USB-6008 is a low-cost, multifunction DAQ I/O device. It consists of analog and digital I/O ports latched with a 32-bit counter. The advantage of the device is that it is easy to connect the terminals and make a compact construction. It is also fitted with advanced NI-DAQmx drivers and NI SignalExpress LE for direct data collection without any need for software triggers and synchronization. Figure 3.24 shows the control panel of the DAQ. The NI USB-6008 specifications are provided in Table 3.5.

Table 3.5 Specifications of NI USB-6008 Data Acquisition system

Analog inputs (Differential)	4
Analog inputs (Single-ended)	8
Input resolution (Differential)	12 bits
Input resolution (Single-ended)	11 bits
Digital I/O	12
Analog output	2
Maximum sample rate	10 KS/s
Timing resolution	41.67 ns (24 MHz timebase)
Timing accuracy	100 ppm of sample rate
Input range (Differential)	$\pm 1V$ to $\pm 20V$
Input range (Single-ended)	$\pm 10V$
Working voltage	$\pm 10V$
Input impedance	$144k\Omega$

The Pin description of NI USB – 6008 is provided in Figure 3.25.

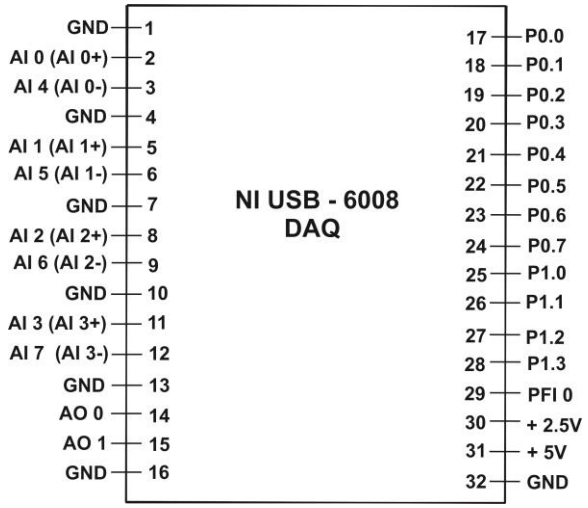

Figure 3.25 Pin description of NI USB – 6008 where AI – analog input, AO – analog output, P I/O – digital I/O and GND – ground.

3.3.3 Correction for scattering volume and detector angle

It is well known that light scattering measurements depends on the scattering volume, detector angles and laser beam width along with the scattering properties and scattering angles. It is practically very easy to understand that during a scattering event as the detector

rotates on the scattering plane, the scattering volume as viewed by the detector as well as the detectable signal intensity varies. These values are different for different positions of the detector on the scattering plane. A maximum overlap of the scattering volume and detector viewing area is possible only for the extreme forward and backward directions (0° and 180°), while it is minimum for absolute perpendicular angle or position i.e. 90°. Therefore it is convenient to multiply the entire detected intensities at all scattering angles by a factor $\sin\theta$ to ensure a constant scattering volume for all detector viewing positions [29, 33, 36, 39, 44].

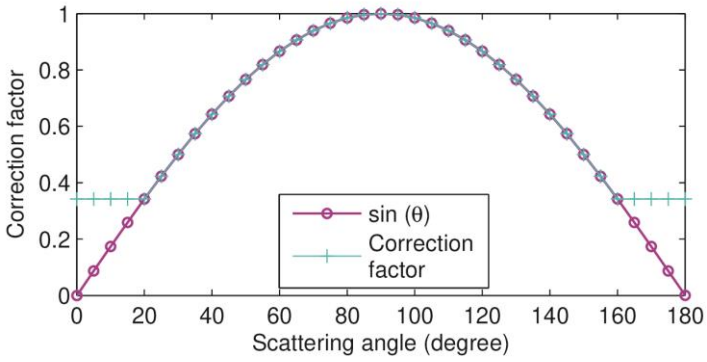

Figure 3.26 Correction factor for scattering volume.

Figure 3.26 shows the correction factor for scattering volume which is almost equal to the $\sin\theta$ function for majority of the scattering angles.

3.3.4 Calibration of the light scattering setup

The calibration process starts with alignment of the various active optical components in the setup namely lasers, photodiodes, polarizers, analyzers, filters and collimators. These components of the setup are mounted on special flexible tables fitted with adjustable screws and lab jacks. By using highly directional test beams from the laser diodes the alignments of the elements are individually checked and adjusted by levelling micrometer screws. The detector rotation axis and the laser beam directions are aligned by putting a temporarily black screen oriented in the axis position, in the scattering plane [29, 36]. The next step is the correction for background noise and stray signals contributed by dust particles contaminating the scattering volume. A high power suction pump is used to force out dust particles that may be present in the scattering chamber. This significantly reduces the intensity of background or dark signals. Further to ensure higher accuracy of the experimental data a number of repetitions (about 100) of the experiments are for each of

the data sets [43]. The background signals are first measured by allowing the laser beam to pass through the scattering volume without any scattering particle. These signals are then subtracted from the results acquired with the scatterer.

$$Data_{(Corrected)} = Data_{(Scatterer)} - Data_{(Background)} \quad \textbf{3.21}$$

A test for the applicability of the experimental setup is conducted for perfectly spherical water droplets sprayed into the scattering volume using a medical nebulizer. To verify the experimental data, the computations performed on the water droplets are carried out using the TUSCAT software [45].

The instrumental errors are calculated by conducting 100 sets of experiments with the water samples of radius 0.5 to 5 μm. As measured from the data sets it is found to be ± 0.194 in arbitrary units. The instrumental errors are plotted as error bars in the experimental plots of all the comparative analysis graphs.

Further for accuracy estimation of the computational and experimental results and for validation of the computational techniques, the Root Mean Square Errors or RMS errors are measured.

$$Error_{rms} = \sqrt{\frac{\sum_{i=1}^{N}(T-E)^2}{N}} \quad \textbf{3.22}$$

Where T and E are theoretical and experimentally measured values and N is the total number of data points.

Table 3.6 provides the properties of the water sample used for the computations.

Table 3.6 Particle size distribution for water droplets

Size Distribution	**Lognormal(Gaussian)**
Lowest particle radius	0.5 μm
Highest particle radius	5.0 μm
Modal radius (r_g)	2.0 μm
Standard deviation (σ_g)	1

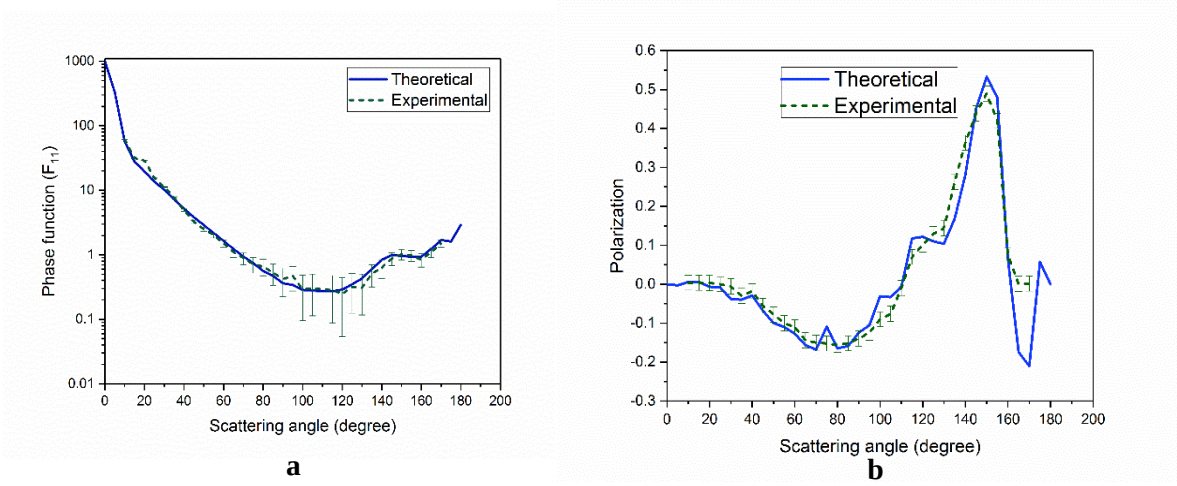

Figure 3.27 (a) Phase function and (b) polarization for water droplets at 543.5 nm wavelength with symbols in the legends representing computational and experimental values (plotted with error bars).

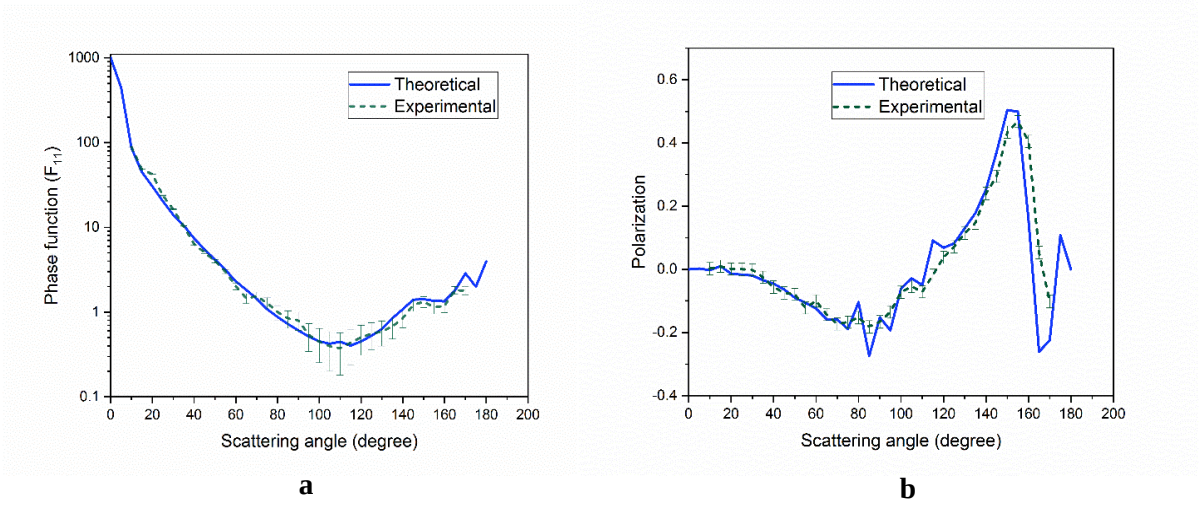

Figure 3.28 (a) Phase function and (b) polarization for water droplets at 594.5 nm wavelength with symbols in the legends representing computational and experimental values (plotted with error bars).

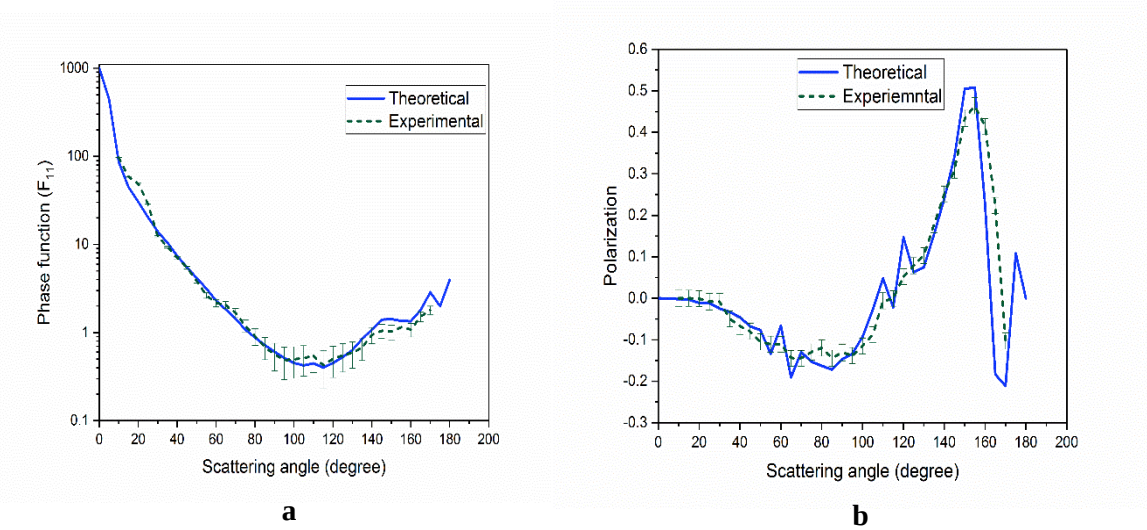

Figure 3.29 (a) Phase function and (b) polarization for water droplets at 632.8 nm wavelength with symbols in the legends representing computational and experimental values (plotted with error bars).

It is observed from the comparative analyses that the experimental plots are almost identical in terms of overall shapes and major features with the computational results for both the measured quantities, which are phase function and degree of linear polarization. The samples considered here are water droplets of perfect spherical shapes, so the effects of only size distributions have been taken into account. Also the computations are carried out using TUSCAT software which incorporates Mie theory and T-Matrix to calculate scattering parameters of spheres and which provides relatively accurate solutions. Therefore with this comparative analyses, applicability of the experimental setup could be verified and it is found to be efficient enough to further carry out investigation of more complex samples.

References

1. Draine, B.T. and Goodman, J., Beyond Clausius-Mossotti-Wave propagation on a polarizable point lattice and the discrete dipole approximation. *The Astrophysical Journal*, 405:685-697, 1993.
2. Draine, B.T. and Flatau, P.J. Discrete-dipole approximation for scattering calculations. *JOSA A*, 11(4) :1491-1499, 1994
3. Draine, Bruce T. *The discrete dipole approximation for light scattering by irregular targets. Light scattering by nonspherical particles: theory, measurements, and applications*, San Diego: Academic Press, 131, 2000.
4. Penttilä, A., Zubko, E., Lumme, K., Muinonen, K., Yurkin, M.A., Draine, B., Rahola, J., Hoekstra, A.G. and Shkuratov, Y., Comparison between discrete dipole implementations and exact techniques. *Journal of Quantitative Spectroscopy and Radiative Transfer*, 106(1-3):417-436, 2007.
5. Wriedt, T. and Comberg, U., Comparison of computational scattering methods. *Journal of Quantitative Spectroscopy and Radiative Transfer*, 60(3):411-423, 1998.
6. Lumme, K. and Rahola, J., Comparison of light scattering by stochastically rough spheres, best-fit spheroids and spheres. *Journal of Quantitative Spectroscopy and Radiative Transfer*, 60(3):439-450, 1998.
7. Xu, Y.L. and Gustafson, B.Å., Comparison between multisphere light-scattering calculations: rigorous solution and discrete-dipole approximation. *The Astrophysical Journal*, 513(2):894, 1999.
8. Yurkin, M.A. and Hoekstra, A.G., The discrete dipole approximation: an overview and recent developments. *Journal of Quantitative Spectroscopy and Radiative Transfer*, 106(1-3):558-589, 2007.
9. Mishchenko, Michael I., Joachim W. Hovenier, and Larry D. Travis, eds. *Light scattering by nonspherical particles: theory, measurements, and applications*. Academic press, 1999.
10. Yurkin, M.A., Maltsev, V.P. and Hoekstra, A.G., Convergence of the discrete dipole approximation. I. Theoretical analysis. *JOSA A*, *23*(10):2578-2591, 2006.
11. Comberg, U. and Wriedt, T., Comparison of scattering calculations for aggregated particles based on different models. *Journal of Quantitative Spectroscopy and Radiative Transfer*, 63(2-6):149-162, 1999.

12. Yurkin, M.A., Hoekstra, A.G., Brock, R.S. and Lu, J.Q., Systematic comparison of the discrete dipole approximation and the finite difference time domain method for large dielectric scatterers. *Optics express*, 15(26):17902-17911, 2007.
13. Pabst, W. and Gregorova, E., Characterization of particles and particle systems. *Prague: ICT*, 27-29, 2007.
14. Kimura, H. and Mann, I., Radiation pressure cross section for fluffy aggregates. *Journal of Quantitative Spectroscopy and Radiative Transfer*, 60(3):425-438, 1998.
15. Kim, S.H. and Martin, P.G., The size distribution of interstellar dust particles as determined from polarization: Spheroids. *The Astrophysical Journal*, 444:293-305, 1995.
16. Krotkov, N.A., Flittner, D.E., Krueger, A.J., Kostinski, A., Riley, C., Rose, W. and Torres, O., Effect of particle non-sphericity on satellite monitoring of drifting volcanic ash clouds. *Journal of Quantitative Spectroscopy and Radiative Transfer*, 63(2-6):613-630, 1999.
17. Mishchenko, M. I., Travis, L. D., Kahn, R. A., West, R. A., Modeling phase functions for dustlike tropospheric aerosols using shape mixture of randomly oriented polydisperse spheroids. *J. Geoph. Res*., 102:16831-16847, 1997.
18. Brownlee, D. E., Pilachowski, L., Olszewski, E., Hodge, P. W., Analysis of interplanetary dust collections. In: Halliday I. and McIntosh B. A. (Eds.), *Solid Particles in the Solar System*. D. Reidel, Dordrecht, 333-342, 1980.
19. Levasseur-Regourd, A.C., Mukai, T., Lasue, J. and Okada, Y., Physical properties of cometary and interplanetary dust. *Planetary and Space Science*, 55(9):1010-1020, 2007.
20. Draine, B. T., and Lee, H. M. Optical properties of interstellar graphite and silicate grains. *The Astrophysical Journal*, 285:89-108, 1984.
21. Mathis, J.S., Rumpl, W. and Nordsieck, K.H., 1977. The size distribution of interstellar grains. *The Astrophysical Journal*, *217*, pp.425-433.
22. Ahmed, G. A. *Design considerations of a laser based air quality monitoring system coupled to a microprocessor linked data recording and processing unit*, PhD thesis, Gauhati University, Guwahati, 2001.

23. Mishchenko, M. I., Travis, L. D., Lacis, A. A. *Scattering absorption and emission of light by small particles,* Electronic Edition, Goddard Institute for Space Studies, New York, 2004 url: http://www.giss.nasa.gov/~crmim/books.html.
24. Hess, M., Koepke, P. and Schult, I., Optical properties of aerosols and clouds: The software package OPAC. *Bulletin of the American meteorological society*, 79(5):831-844, 1998.
25. Winstanley, J.V. and Adams, M.J., Point visibility meter: a forward scatter instrument for the measurement of aerosol extinction coefficient. *Applied optics*, 14(9):2151-2157, 1975.
26. Vaz, M.F. and Fortes, M.A., Grain size distribution: The lognormal and the gamma distribution functions. *Scripta metallurgica*, 22(1):35-40, 1988.
27. Hansen, J. E. and Travis, L. D. Light scattering in planetary atmospheres. *Space Sci. Rev.*, 16(4):527-610, 1974.
28. Kokhanovsky, A. A. *Aerosol Optics Light Absorption and Scattering by Particles in the Atmosphere,* Praxis Publishing Ltd, Chichester, UK, 2008
29. Jonasz, M. and Fournier G. R. *Light Scattering by Particles in Water Theoretical and Experimental Foundations,* Elsevier, Amsterdam, 2007.
30. Chen, K., Kromin, A., Ulmer, M.P., Wessels, B.W. and Backman, V., Nanoparticle sizing with a resolution beyond the diffraction limit using UV light scattering spectroscopy. *Optics Communications*, 228(1-3):1-7, 2003.
31. Heintzenberg, J., Properties of the log-normal particle size distribution, *Aerosol Science and Technology*, 21(1):46-48, 1994.
32. Van de Hulst, H.C. *Light Scattering by Small Particles,* Dover Publications, New York, 1981.
33. Bohren, C.F., and Huffman, D.R. *Absorption and scattering by a sphere.* Wiley-VCH Verlag GmbH, 1983.
34. Petzold, T.J., *Volume scattering functions for selected ocean waters* (No. SIO-REF-72-78). Scripps Institution of Oceanography La Jolla Ca Visibility Lab, 1972.
35. Jonasz, M. *Size, shape, composition, and structure of microparticles from light scattering. In: principles, methods, and application of particle size analysis,* Editor: Syvtsky, J. P. M., Cambridge University Press, Cambridge, 1991.

36. Gogoi, A. *Characterization of small particulate matter by using an indigenously designed laser based probe and development of relevant software*, PhD thesis, Tezpur University, Tezpur, (2011).
37. Hapke, B.W., Nelson, R.M. and Smythe, W.D., The opposition effect of the moon: the contribution of coherent backscatter. *Science*, 260(5107):509-511, 1993.
38. McGuire, A.F. and Hapke, B.W., An experimental study of light scattering by large, irregular particles. *Icarus*, 113(1):134-155, 1995.
39. Volten, H., De Haan, J.F., Hovenier, J.W., Schreurs, R., Vassen, W., Dekker, A.G., Hoogenboom, H.J., Charlton, F. and Wouts, R., Laboratory measurements of angular distributions of light scattered by phytoplankton and silt. *Limnology and oceanography*, 43(6):1180-1197, 1998.
40. Hovenier, J.W., Van de Hulst, H.C. and Van der Mee, C.V.M., Conditions for the elements of the scattering matrix. *Astronomy and Astrophysics*, 157:301-310, 1986.
41. Munoz, O., Volten, H., De Haan, J.F., Vassen, W. and Hovenier, J.W., Experimental determination of the phase function and degree of linear polarization of El Chichon and Pinatubo volcanic ashes. *Journal of Geophysical Research: Atmospheres*, 107(D13), 2002.
42. Hovenier, J.W., Volten, H., Munoz, O., Van der Zande, W.J. and Waters, L.B.F.M., Laboratory studies of scattering matrices for randomly oriented particles: potentials, problems, and perspectives. *Journal of Quantitative Spectroscopy and Radiative Transfer*, 79:741-755, 2003.
43. Gogoi, A., Borthakur, L.J., Choudhury, A., Stanciu, G.A. and Ahmed, G.A., Detector array incorporated optical scattering instrument for nephelometric measurements on small particles. *Measurement Science and Technology*, 20(9):095901, 2009.
44. O'Bree, T. A. *Investigations of light scattering by Australian natural waters for remote sensing applications.* PhD thesis, School of Applied Sciences, Applied Physics, RMIT University, Victoria, Australia, 2007.
45. Gogoi, A., Rajkhowa, P., Choudhury, A. and Ahmed, G.A., Development of TUSCAT: A software for light scattering studies on spherical, spheroidal and cylindrical particles. *Journal of Quantitative Spectroscopy and Radiative Transfer*, 112(17):2713-2721, 2011.